High-spectral-resolution terahertz imaging with a quantum-cascade laser

Till Hagelschuer,[1,*] Nick Rothbart,[1,2] Heiko Richter,[1] Martin Wienold,[1,2] Lutz Schrottke,[3] Holger T. Grahn,[3] and Heinz-Wilhelm Hübers[1,2]

[1]*German Aerospace Center (DLR), Institute of Optical Sensor Systems, Rutherfordstr. 2, 12489 Berlin, Germany*
[2]*Humboldt-Universität zu Berlin, Department of Physics, Newtonstr. 15, 12489 Berlin, Germany*
[3]*Paul-Drude-Institut für Festkörperelektronik, Leibniz-Institut im Forschungsverbund Berlin e. V., Hausvogteiplatz 5–7, 10117 Berlin, Germany*
[*]*Till.Hagelschuer@DLR.de*

Abstract: We report on a high-spectral-resolution terahertz imaging system operating with a multi-mode quantum-cascade laser (QCL), a fast scanning mirror, and a sensitive Ge:Ga detector. By tuning the frequency of the QCL, several spectra can be recorded in 1.5 s during the scan through a gas cell filled with methanol (CH_3OH). These experiments yield information about the local absorption and the linewidth. Measurements with a faster frame rate of up to 3 Hz allow for the dynamic observation of CH_3OH gas leaking from a terahertz-transparent tube into the evacuated cell. In addition to the relative absorption, the local pressure is mapped by exploiting the effect of pressure broadening.

OCIS codes: (110.6795) Terahertz imaging; (140.5965) Semiconductor lasers, quantum cascade; (300.6495) Spectroscopy, terahertz.

References and links

1. M. Tonouchi, "Cutting-edge terahertz technology," Nat. Photonics 1(2), 97–105 (2007).
2. F. C. De Lucia, "Spectroscopy in the Terahertz Spectral Region," in *Sensing with Terahertz Radiation*, D. Mittleman, ed. (Springer, 2003).
3. H. Richter, M. Wienold, L. Schrottke, K. Biermann, H. T. Grahn, and H.-W. Hübers, "4.7-THz local oscillator for the GREAT heterodyne spectrometer on SOFIA," IEEE Trans. Terahertz Sci. Technol. **5**(4), 539–545 (2015).
4. L. Rezac, P. Hartogh, R. Güsten, H. Wiesemeyer, H.-W. Hübers, C. Jarchow, H. Richter, B. Klein, and N. Honingh, "First detection of the 63 µm atomic oxygen line in the thermosphere of Mars with GREAT/SOFIA," Astron. Astrophys. **580**, L10 (2015).
5. A. M. Fosnight, B. L. Moran, and I. R. Medvedev, "Chemical analysis of exhaled human breath using a terahertz spectroscopic approach," Appl. Phys. Lett. **103**(13), 133703 (2013).
6. A. G. Davies, A. D. Burnett, W. Fan, E. H. Linfield, and J. E. Cunningham, "Terahertz spectroscopy of explosives and drugs," Mater. Today **11**(3), 18–26 (2008).
7. J. Liu, W.-H. Fan, X. Chen, and J. Xie, "Identification of high explosive RDX using terahertz imaging and spectral fingerprints," J. Phys. Conf. Ser. **680**, 012030 (2016).
8. P. F.-X. Neumaier, K. Schmalz, J. Borngräber, R. Wylde, and H.-W. Hübers, "Terahertz gas-phase spectroscopy: chemometrics for security and medical applications," Analyst (Lond.) **140**(1), 213–222 (2015).
9. E. Bründermann, H.-W. Hübers, and M. Kimmitt, *Terahertz Techniques* (Springer, 2012).
10. K. Kawase, Y. Ogawa, Y. Watanabe, and H. Inoue, "Non-destructive terahertz imaging of illicit drugs using spectral fingerprints," Opt. Express **11**(20), 2549–2554 (2003).
11. Y. C. Shen, T. Lo, P. F. Taday, B. E. Cole, W. R. Tribe, and M. C. Kemp, "Detection and identification of explosives using terahertz pulsed spectroscopic imaging," Appl. Phys. Lett. **86**(24), 241116 (2005).
12. Y. C. Shen, L. Gan, M. Stringer, A. Burnett, K. Tych, H. Shen, J. E. Cunningham, E. P. J. Parrott, J. A. Zeitler, L. F. Gladden, E. H. Linfield, and A. G. Davies, "Terahertz pulsed spectroscopy imaging using optimized binary masks," Appl. Phys. Lett. **95**(23), 231112 (2009).
13. P. Dean, N. K. Saat, S. P. Khanna, M. Salih, A. Burnett, J. Cunningham, E. H. Linfield, and A. G. Davies, "Dual-frequency imaging using an electrically tunable terahertz quantum cascade laser," Opt. Express **17**(23), 20631–20641 (2009).

14. M. Wienold, L. Schrottke, M. Giehler, R. Hey, W. Anders, and H. T. Grahn, "Low-voltage terahertz quantum-cascade lasers based on LO-phonon-assisted interminiband transitions," Electron. Lett. **45**(20), 1030–1031 (2009).
15. H. Richter, M. Greiner-Bär, S. G. Pavlov, A. D. Semenov, M. Wienold, L. Schrottke, M. Giehler, R. Hey, H. T. Grahn, and H.-W. Hübers, "A compact, continuous-wave terahertz source based on a quantum-cascade laser and a miniature cryocooler," Opt. Express **18**(10), 10177–10187 (2010).
16. N. Rothbart, H. Richter, M. Wienold, L. Schrottke, H. T. Grahn, and H.-W. Hübers, "Fast 2-D and 3-D terahertz imaging with a quantum-cascade laser and a scanning mirror," IEEE Trans. Terahertz Sci. Technol. **3**(5), 617–624 (2013).
17. G. Moruzzi, P. Riminucci, F. Strumia, B. Carli, M. Carlotti, R. M. Lees, I. Mukhopadhyay, J. W. C. Johns, B. P. Winnewisser, and M. Winnewisser, "The spectrum of CH_3OH between 100 and 200 cm^{-1}: Torsional and "forbidden" transitions," J. Mol. Spectrosc. **144**(1), 139–200 (1990).

1. Introduction

Due to a variety of molecular rotational and atomic fine structure lines, spectroscopy in the terahertz (THz) spectral region is a powerful tool. It can be applied to detect and identify numerous chemical compounds in particular gases. Thus, it holds a large potential for a broad range of applications e.g. in astrophysics, medicine, and security [1,2]. In astrophysics, molecular rotational and atomic fine structure transitions enable the investigation of planetary atmospheres and the interstellar medium. A recent example is the detection of the $^3P_1 \rightarrow {}^3P_2$ transition at 4.7 THz of neutral atomic oxygen OI with a heterodyne spectrometer onboard of the Stratospheric Observatory for Infrared Astronomy [3,4]. In medicine, the same principle is exploited to diagnose cancer, e.g. by spectral analysis of the breathing gas [5]. In security, explosives and poisonous gases can be identified by their characteristic absorption peaks in the THz range [6–8].

At present, THz imaging is realized with a variety of different techniques [9]. However, relatively little work has been reported regarding the combination of THz spectroscopy with imaging. One of the first experiments on this topic relied on a THz-wave parametric oscillator. With this frequency-tunable source, spectrally resolved THz images of illicit drugs have been obtained [10]. In addition, THz time domain systems have been used for spectral THz imaging [11,12]. Some limited spectroscopic information has been obtained by employing a THz quantum-cascade laser (QCL) for dual-frequency imaging [13]. These approaches have in common that they provide rather low-spectral-resolution images with a resolving power on the order of 100 or with just two frequencies.

In this study, we will present a QCL-based spectrometer that is capable of fast spectral imaging with a resolving power on the order of 10^6 and with a high spatial resolution. The very large spectral resolving power of this approach together with the high spatial resolution and fast measurement time opens the path to sophisticated in situ, real-time analysis of the dynamics of gases far beyond the mere identification of the gases species. While the spectral information is obtained by frequency tuning of the QCL, frame rates of up to 3 Hz are realized by the combination of a fast scanning mirror (FSM), a scan of the THz beam across the sample, and a sensitive single-pixel Ge:Ga detector with a short response time. We first describe the experimental setup and discuss its characteristics and performance. This is followed by the analysis of the spectral absorption images based on a CH_3OH Q-branch molecular rotational transition at approximately 3.4 THz. By exploiting the pressure broadening effect, we derive the local pressure from the spectral linewidth.

2. Experimental setup

A schematic overview of the imaging system is given in Fig. 1. THz radiation is generated by a multi-mode QCL based on a GaAs/(Al,Ga)As active region heterostructure and a single-plasmon waveguide. Details of the active region are described in [14]. The QCL is mounted in a compact Stirling cryocooler (Ricor K535) and operated at a temperature of 40 K [15]. The exit window is made of high-density polyethylene (HDPE). Depending on the laser driving current, up to five Fabry-Pérot laser modes separated by approximately 32.6 GHz are

simultaneously emitted in the range from 3.3 to 3.5 THz. At the current-tempererature setting used for spectral imaging, the spectrum is dominated by one laser mode at approximately 3.4 THz (inset in Fig. 1). The DC current for the QCL is provided by a laser driver (ILX Lightwave LDX-3232). In order to obtain spectral information, the frequency of the QCL is tuned by a sawtooth-like current pattern in a range which covers the spectral feature of interest within the detection time of one pixel. For a molecular absorption line which is typically a few MHz broad, this corresponds to a current modulation with an amplitude of approximately 10 mA. For lock-in detection, a voltage modulation with a frequency of 300 kHz is applied to the modulation input of the driver. This results in a 300 kHz current modulation, which is superimposed on the sawtooth pattern. Since the frequency of the QCL changes with temperature, the heat sink temperature is stabilized with an accuracy of ± 5 mK by a temperature control unit (CryoCon C24).

The QCL beam is collimated by a plano-convex poly-4-methylpentene-1 (TPX) lens with a diameter of 50 mm and a focal length of 92 mm. At a distance of 322 mm from the exit window, the beam incides at an angle of 20° on a 35-mm diameter fast scanning mirror (FSM). The FSM can be tilted by ± 3° in vertical and horizontal direction with a resolution of 2 µrad. This corresponds to a spatial separation of approximately 1 µm in the object plane. The position of the FSM is controlled by a dedicated electronic controller, which in turn is operated by a software package and read out by a data acquisition device (DAQ). We used a spiral scan with linearly increasing frequency to steer the FSM from outward to inward across the object. During the scan, the spectral information is obtained by continuously varying the QCL current. The beam reflected by the FSM is focused by a plano-convex HDPE lens with a focal length of 250 mm and a diameter of 76 mm. The beam is directed through a 72.5-mm long absorption cell with an inner diameter of 45 mm sealed by 1.5-mm thick HDPE windows. In order to avoid standing waves, the windows of the absorption cell are tilted with respect to the optical axis. CH_3OH is injected into the absorption cell via a needle valve (V_1) and evacuated by a turbomolecular pump (TMP), which is connected to the cell by a second valve (V_2). For spectral imaging, a tube is mounted in the object plane inside the absorption cell (cf. Fig. 1), which is made of THz-transparent poly-4-fluorethylen (PTFE) with an outer diameter of 8 mm, an inner diameter of 6 mm, and a length of 24 mm. At the ends of the tube, two THz absorbing flexible pieces made of hollow rubber ensure a tight connection to V_1 and another valve V_3, which is connected to the TMP. In this configuration, the gas flow is confined to the interior of the tube. The base pressure of the evacuated absorption cell is10^{-3} hPa, the base pressure inside the PTFE tube is 10^{-2} hPa.
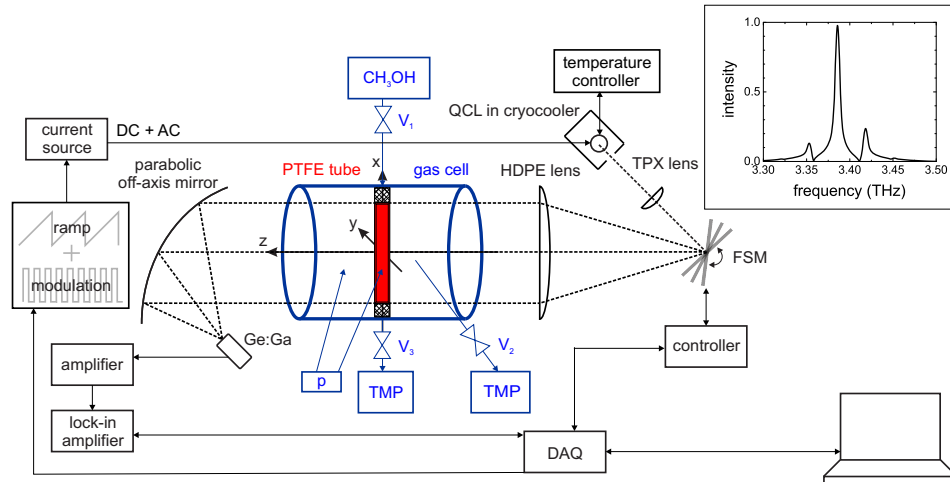
Fig. 1. Schematic of the spectral imaging setup. THz radiation emitted by a QCL is scanned through an absorption cell by a fast scanning mirror (FSM). The beam is focused on a THz-transparent PTFE tube filled with CH_3OH inside the cell (indicated by the red rectangle). The transmitted radiation is detected with a Ge:Ga detector.

A 76-mm focal length off-axis parabolic mirror focuses the transmitted beam on a Ge:Ga photoconductive detector. The detector signal is amplified (Stanford Research Systems SR560) and fed into a phase-sensitive lock-in amplifier (Zurich Instruments HF2) taking the QCL modulation frequency as a reference. The signal is read out by the DAQ.

3. Optical properties and QCL characterization

The spatial resolution achievable with this setup depends primarily on the quality of the beam profile. As described in [16], the beam profile is measured with a mid-infrared microbolometer camera (Infratec Variocam), which has been modified for THz applications. Figure 2(a) shows a beam profile at the intersection of the optical axis with the object plane. The full width at half maximum (FWHM) is 0.6 mm in the horizontal as well as in the vertical direction. There are some fringes, which are due to diffraction at the TPX lens. To obtain more information about the image quality, the contrast is determined using a grid of metal bars with a width of 1 mm and 5 lines per cm, which is moved along the optical axis z (cf. Fig. 1). The contrast C is calculated according to

$$C = \frac{I_{max} - I_{min}}{I_{max} + I_{min}}, \tag{1}$$

with I_{max} and I_{min} denoting the average values of the maximum and minimum intensities. The contrast function $C(z)$ is plotted in Fig. 2(b), indicating a maximum horizontal and vertical contrast of 0.49 and 0.56, respectively, in the focal plane ($z = 0$). At the edges of the absorption cell, the horizontal and vertical contrast is 0.36 and 0.36, respectively, at the front as well as 0.30 and 0.33, respectively, at the rear edge of the cell.

In order to determine the absolute frequency and the frequency tuning of the QCL with respect to its driving current and temperature, the absorption spectrum of CH_3OH has been measured at a pressure of 5 hPa. Fast sweeping of the QCL current in the range from 570 to 600 mA and simultaneous recording of its temperature allows for a mapping of the transmission signal as a function of current and temperature as shown in Fig. 3(a). From the position of the absorption lines – in this case three – in the current-temperature map, the frequency tuning coefficients can be determined. The details of this procedure are described

in [3]. In the vicinity of an absorption line, the QCL frequency v is well described by a linear dependence on the driving current and the heat sink temperature. The frequency tunability
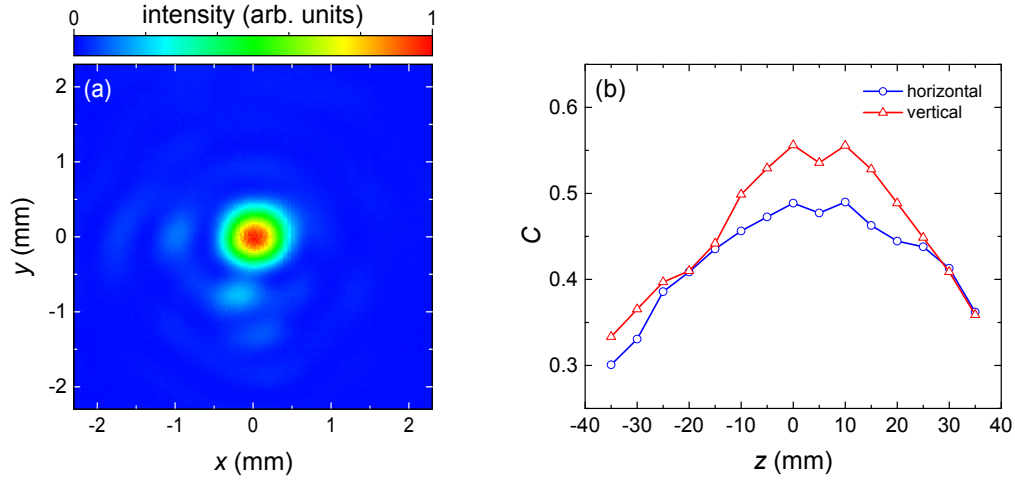

Fig. 2. (a) Beam profile at the center position ($x = y = z = 0$) of the object plane inside the absorption cell and (b) contrast function $C(z)$ along the optical axis.
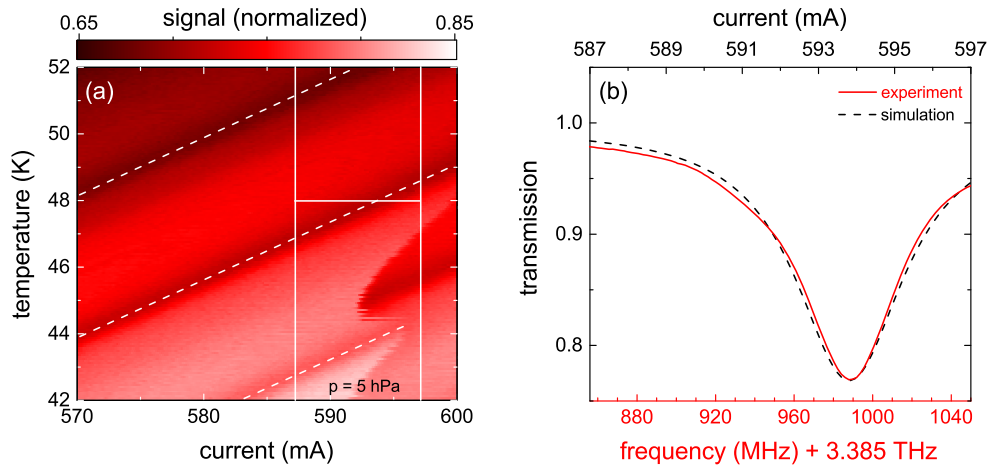

Fig. 3. (a) Signal transmitted through the absorption cell which is filled with CH_3OH at a pressure of 5 hPa as a function of driving current and heat sink temperature of the QCL. The operating range applied for spectral imaging is indicated by the vertical lines. Around 595 mA and below 47 K, a mode jump occurs. (b) The transmission spectrum which corresponds to the white horizontal line in (a). The red line indicates the measured absorption, while the dashed line is a result of a simulation.

with current is (19.4 ± 0.4) MHz/mA, and the frequency tunability with temperature amounts to (-112.5 ± 5.8) MHz/K. Because of this dependence, an accurate stabilization of the QCL temperature is an important necessity. For spectral imaging, the QCL current is sawtooth-modulated from 587 to 597 mA, keeping the heat sink temperature at 48 K as indicated by the solid lines in Fig. 3(a). In this region, the THz radiation is primarily emitted in a single mode at approximately 3.39 THz. At 593.8 mA, a transmission minimum is observed [cf. Fig. 3(b)]. Following the notation in [17], it is identified as the $Q(1,7;21)^0 \leftarrow (1,6;21)^0A$ rotational transition of CH_3OH at 3.38599 THz.

4. Transmission-based spectral imaging

Spectral imaging of molecules can be based on the change of the transmission at a fixed frequency, preferably at the central frequency of the molecular absorption line, or of the integral absorption of the molecular line. Alternatively, the linewidth can be used for spectral imaging. Both approaches yield different information, because the absorption depends on the total number of molecules along the line-of-sight while the linewidth depends on the local concentration of molecules. Measuring the integral absorption or the linewidth requires a frequency scan across the absorption line. Here, we focus on transmission-based spectral imaging using peak absorption. The spectrum presented in Fig. 3(b) is measured at a pressure of 5 hPa. At this pressure, the lineshape with a FWHM of 67.5 MHz is dominated by pressure broadening, since the Doppler width of a CH_3OH absorption line at this frequency and 300 K is 7.4 MHz. Therefore, the effect of Doppler broadening is neglected, and the transmission $T(\nu)$ is approximated by a Lorentzian function given by

$$T(\nu) = T_0 - \frac{2Aw}{\pi[4(\nu - \nu_C)^2 + w^2]}. \tag{2}$$

Here, A denotes the integral absorption, w the FWHM, ν_C the central absorption frequency, and T_0 the baseline transmission. From these parameters, the normalized peak absorption A^* at the corresponding frequency is calculated by

$$A^* = \frac{T_0 - T(\nu_C)}{T_0} = \frac{2A}{\pi w T_0}, \tag{3}$$

which is independent of any background absorption, e.g. by the tube, as it is normalized to T_0.

In a first experiment, the tube is filled with CH_3OH via V_1 up to a pressure of 5 hPa. Then all valves are closed. The QCL is continuously swept over 200 MHz. At the same time, the FSM performs a spiral scan trajectory with a sampling rate of 600 kHz. In this configuration, one image with 5,957 spectra is acquired in 1.5 s. The elliptical (long axis 18.2 mm, short axis 17.8 mm) field of view (FoV) consists of 1,350 pixels with 0.5 mm edge length. For each pixel, the spectrum is determined by averaging all spectra along the scan trajectory within a 0.25-mm^2 pixel. Since the quality of the spectral image depends significantly on the number of spectra per pixel, at least four spectra are recorded for each pixel. The resulting image is normalized to a reference image taken with an evacuated absorption cell. This ensures that the absorption originates from CH_3OH and is not affected by absorption from the tube. A spectral image is generated by evaluating the transmission spectra with respect to the peak absorption.

Figure 4(a) presents the resulting absorption image based on the relative absorption A^* determined from the CH_3OH rotational transition shown in Fig. 3. Two different regions labelled A ($x < -5$ mm and $x > 3$ mm) and B (-4 mm $< x < 2$ mm) can be distinguished. In region A, which is identical to the absorption cell outside the PTFE tube, only a small absorption of less than 0.02 is detected. In region B, which is the inner part of the PTFE tube, the absorption is 0.07 and rather homogeneous. The narrow transition zones between A and B are due to the wall of the tube. Typical spectra of regions A and B are plotted in Fig. 4(b). As a result of some residual CH_3OH, the absorption in region A is not exactly zero. However, it is significantly less than in region B, especially if the much smaller absorption length is taken into account. The transmission spectrum of region B is well approximated by a Lorentzian line according to Eq. (2).

To demonstrate the potential of fast spectral imaging, a circular hole of 0.2 mm diameter is drilled in the center of the tube. Prior to injection of CH_3OH, the tube and the absorption cell are evacuated. Then the valves V_2 and V_3 are closed, and CH_3OH is injected via V_1. In order to capture the dynamics of the gas outpouring from inside the tube into the absorption

cell, the whole area is continuously imaged. The maximum FSM deflection angle is set to $\pm$ 0.5° to shorten the acquisition time to 0.33 s per image. The FoV (long axis 8.9 mm, short axis 8.7 mm) consists of 367 pixels and contains 1,997 spectra, i.e. at least five spectra per pixel.
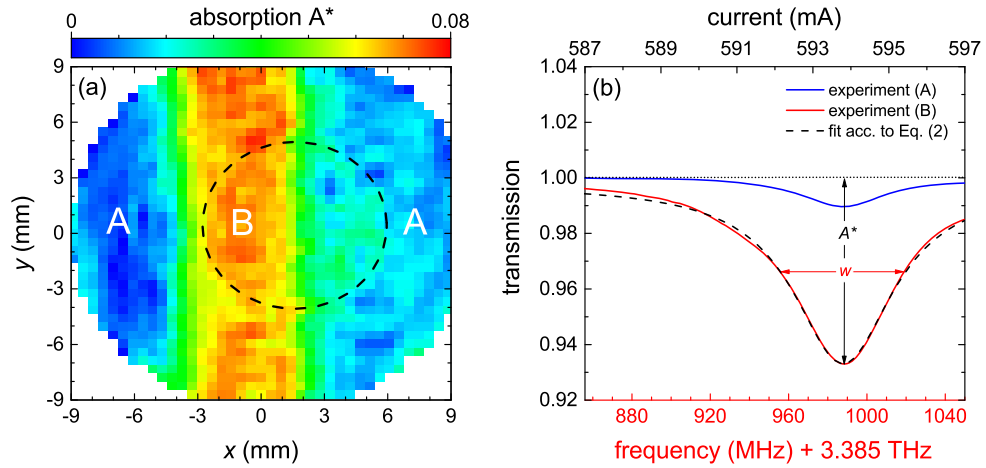

Fig. 4. (a) Spectral absorption image of CH_3OH with the PTFE tube visible by the higher absorption (yellow-red region). The spectral image consists of 1,350 pixels and was acquired within 1.5 s. (b) Absorption spectra of CH_3OH at a pressure of 5 hPa inside (red line) and outside (blue line) of the PTFE tube.
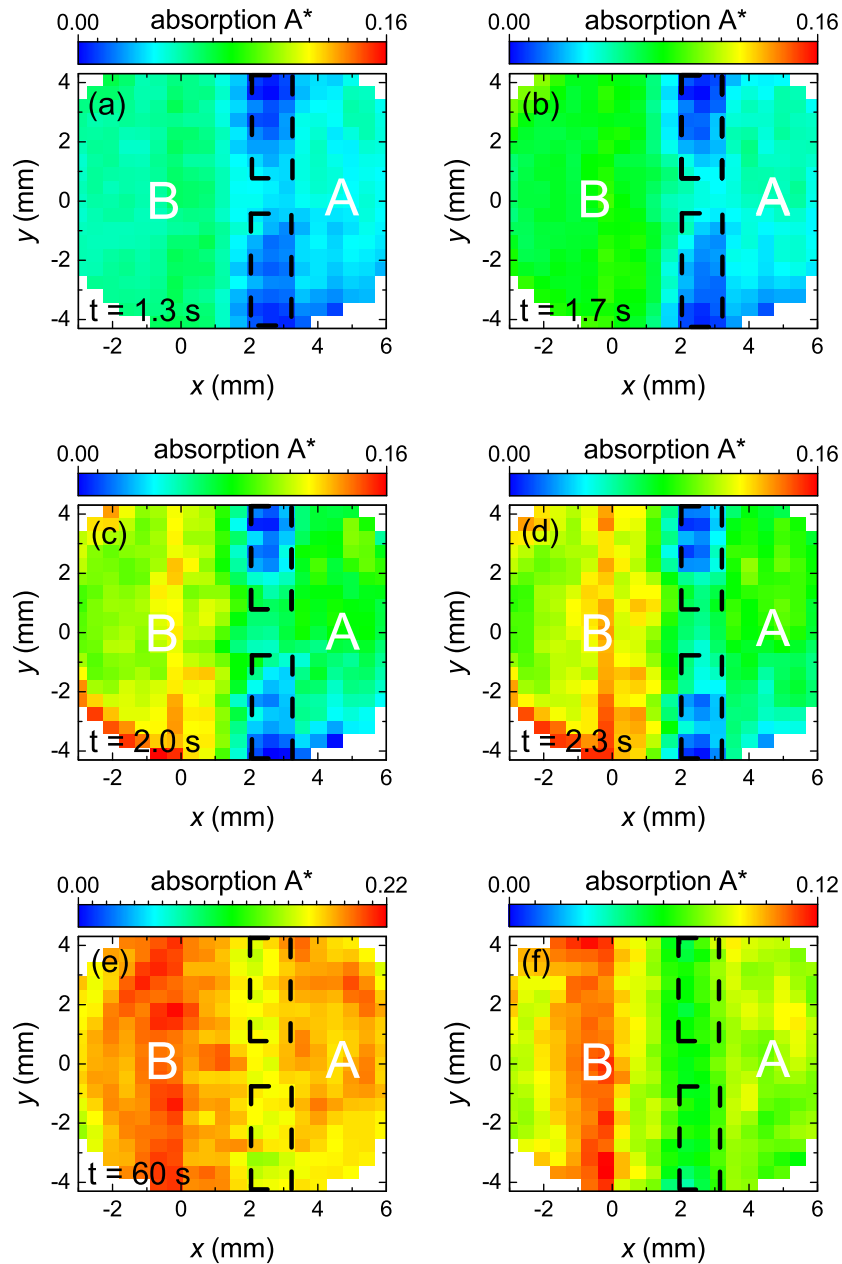
Fig. 5. Sequence of absorption images of the same tube as in shown in Fig. 4(a), where the investigated area is marked by the circle (dashed line). The wall of the tube is indicated by the rectangles (dashed lines). The area between the rectangles is a hole, which was drilled into the tube. Each frame has been recorded within 0.33 s and normalized to the background. (a)−(d) Successive sequence of absorption images starting at t = 1.33 s after gas injection via V_1 at t = 0, showing how the leakage evolves over time. (e) Absorption image at t = 60 s, when the absorption in the tube and the gas cell is almost at equilibrium. (f) Absorption image after opening of V_2. Note that the absorption scale in (e) and (f) is different.

Figures 5(a)–5(d) present a sequence of absorption images of the leaking tube. The image corresponds to the dashed frame in Fig. 4(a). The left area ($x < 2$ mm) of each image belongs to region B, while the right area ($x > 3$ mm) corresponds to region A [labelling as in Fig. 4(a)]. The dark blue region (2 mm $< x <$ 3 mm) between regions A and B in Fig. 5(a) corresponds to the wall of the tube. The light blue zone in Fig. 5(a) (at -0.5 mm $< y < 0.5$ mm) between the two dark blue ones on top and below corresponds to the hole in the wall of the tube. For clarity, the walls of the tube are indicated by dashed lines. At $t = 1.3$ s after opening the CH$_3$OH inlet valve V$_1$, absorption differences of up to 0.05 between regions A and B are detected [cf. Fig. 5(a)]. The absorption in region B increases to 0.1 at $t = 1.7$ s. Note that although the dimension of the hole is below the spatial resolution limit, it can be identified based on the absorption contrast between the gas leak in the tube ($x = 3$ mm, $y = z = 0$ mm) and the high transmission of the tube wall. Maximum absorption values of 0.09 in region A and 0.14 in region B are detected at $t = 2.3$ s. The absorption contrast between regions A and B remains almost constant at about 0.04 [cf. Figs. 5(a)–5(d)], while the total absorption is constantly increasing. This indicates that the gas flow through V$_1$ is similar to the flow through the hole, and the latter one does not act as a bottleneck. After 60 s, the absorption contrast between both regions becomes smaller, and the overall absorption is saturated at 0.20 [cf. Fig. 5(e)]. The process is reversed through evacuation of region A: 1 s after opening V$_2$, the absorption in regions A and B has decreased significantly [cf. Fig. 5(f)].

5. Lineshape-based spectral imaging

Another application of spectral imaging is mapping the pressure of a gas by exploiting the pressure broadening effect. To calibrate the spectral linewidth with the operating pressure, the absorption of the same CH$_3$OH line is measured in the homogenously filled absorption cell without an object inside in a range from 1 to 6 hPa. The spectra are normalized to the maximum absorption [cf. Fig. 6(a)]. The dependence of the linewidth on pressure is shown in Fig. 6(b). The FWHM w depends linearly on the pressure p

$$w(p) = b \cdot p + d. \tag{4}$$

Here, $b = (9.4 \pm 0.5)$ MHz/hPa denotes the pressure broadening coefficient and $d = (7.6 \pm 0.5)$ MHz the FWHM at zero pressure, i.e. the Doppler width of the line, which is close to the predicted value of 7.4 MHz at 300 K. For the frequency calibration, we used the tuning coefficient of (19.4 ± 0.4) MHz/mA.
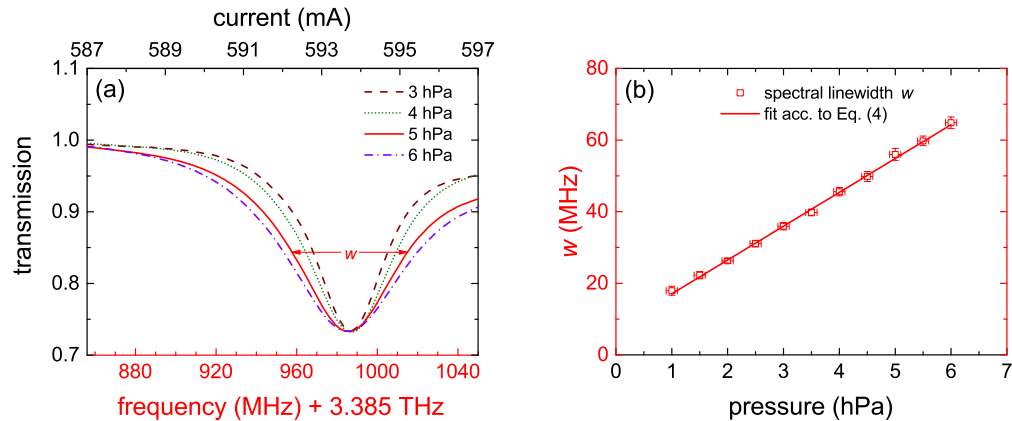

Fig. 6. (a) Absorption spectra of CH$_3$OH at different pressure values. (b) Linewidth w (FWHM) as a function of CH$_3$OH pressure p measured in the homogenously filled gas cell. The function $w(p)$ is approximated by a linear function according to Eq. (4).

To underline the advantage of a spectral image in pressure representation, the leakage experiment demonstrated in Figs. 5(a)−5(d) is repeated. In order to observe pressure deviations between the different regions A and B, the whole area is investigated in a larger FoV and over a longer period of time. Therefore, the FSM deflection angle is adjusted to $\pm 2°$ and the elliptical FoV (long axis 36 mm, short axis 32 mm) consists of 4,370 pixels and contains 4,606 spectra. The experiment is performed as described above, i.e. CH_3OH is injected via V_1 at the same time when the scan is initialized at $t = 0$. The valves V_2 and V_3 remain closed.

Figure 7 presents a comparison between a transmission-based image [cf. Fig. 7(a)] and a linewidth-based image [cf. Fig. 7(b)]. In both images, the tube is visualized by the black lines. The shaded areas mark the hollow rubber pieces at the ends of the tube. Following the notation introduced in Fig. 4(a), A denotes the region outside and B the region inside the PTFE tube. In Fig. 7(a), a maximum absorption of 0.15 is detected in region B. In accordance with the results of Fig. 4(a), a homogenous distribution is determined except for a slightly increasing absorption towards the location of the leak. The latter observation is in accordance with Fig. 5, and the absence of a leak in the first experiment conducted for Fig. 4(a). This effect is not exclusively caused by the temporal convolution of the measurement, since the maximum absorption in B is detected along the entire axis at $x = 0$. This is confirmed by the gas propagation shown in region A. The maximum absorption of 0.14 is detected near the leak and gradually decreases with increasing distance to a minimum of 0.01 at the end of the gas cell. The gas is mostly in the right part of A ($x > 3$ mm), which indicates that the dispersal is rather small during the image acquisition time of 9.7 s.

In Fig. 7(b), the local pressure map of the same measurement is derived from the linewidth w in each spectrum according to Eq. (4). The different colors indicate the pressure levels. In accordance with the result in Fig. 7(a), the maximum pressure of 2.5 hPa is detected in region B in the vicinity of the leak. However, Fig. 7(a) reveals a less pronounced gradient because the absorption is an integral along the line-of-sight while the linewidth is a measure for the local pressure. The pressure in region B gradually decreases to the left edge of the tube to a minimum value of 1.5 hPa. The maximum pressure is measured close to the leakage position ($x = 3$ mm, $y = z = 0$). It is significantly more localized than in the absorption measurement. This is also valid for the gas propagation resolved by the different pressure zones. The pressure gradient in region A decreases from the leakage zone in all spatial directions to a minimum value of 0.8 hPa at the end of the cell, because of the expansion of the gas.
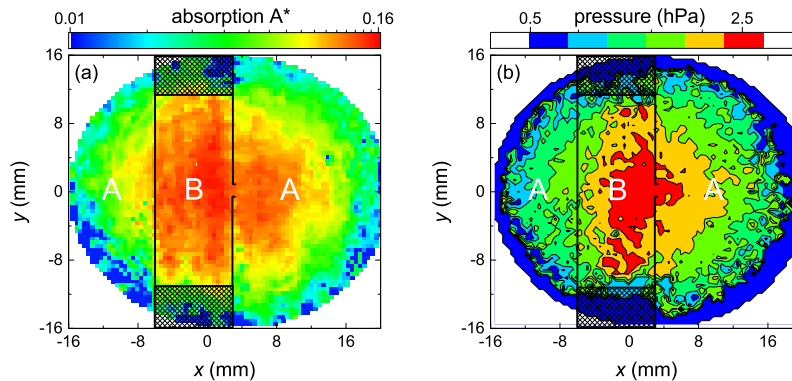

Fig. 7. (a) Spectral image of the leakage process derived from a transmission measurement and (b) from the width of the absorption line which corresponds to the local pressure. The whole area is acquired in 9.7 s and contains 4,606 spectra. The position of the tube is indicated by the black rectangle. While the gas distribution is observed in (a) as well as in (b), the hole where the gas leaks out is better resolved in (b).

6. Summary and conclusion

We have developed a high-spectral-resolution THz imaging setup based on a QCL, a fast scanning mirror, and a single pixel Ge:Ga detector. Images with a spatial resolution of 1 mm or better as well as spectral information with a resolution of 2 MHz are obtained through frequency tuning of the QCL. Almost 6,000 spectra and 1,350 pixels are measured in 1.5 s providing information about the gas concentration and pressure. This information can be deduced from the absorption as well as the linewidth of the molecular transition. The scan time and the spatial resolution are limited by the mechanics of the scanning mirror and the THz beam waist, respectively. The setup allows for the observation of gas dynamics and leak detection as demonstrated with a CH_3OH-filled THz-transparent tube. The system proves the feasibility of fast simultaneous high-resolution spectroscopy and high-resolution imaging at THz frequencies.

Acknowledgment